



# Acoustic Modeling Using the Aeroacoustic Wave Equation Based on Pierce's Operator

Stefan Schoder\*<sup>1</sup>

Graz University of Technology, 8010 Graz, Austria

and

Étienne Spieser,<sup>†</sup> Hugo Vincent,<sup>‡</sup> Christophe Bogey,<sup>§</sup> and Christophe Bailly<sup>§</sup>

University of Lyon, Ecole Centrale de Lyon, CNRS, University of Claude Bernard Lyon 1, INSA Lyon, LMFA, UMR5509, 69130, Écully, France

<https://doi.org/10.2514/1.J062558>

**The capabilities of an aeroacoustic wave equation based on Pierce's operator (AWE-PO) for modeling subsonic flow-induced sound and for sound prediction are investigated. The wave equation is applied to an isothermal two-dimensional mixing layer computed by direct numerical simulation. In contrast to a direct numerical simulation, providing the acoustic fluctuations directly, the simulations based on Lighthill's wave equation and the AWE-PO rely on a hybrid workflow to predict the generated sound field. Special attention is put on the interpretation of the right-hand side of both wave equations. Comparing the terms on the right-hand side in Lighthill's theory and AWE-PO suggests a source amplitude for AWE-PO that is 90% smaller. This reduction is attributed to the filtering property of the material derivative. Finally, the results of the acoustic far-field pressure are compared. It is shown that the radiated sound field's directivity, propagation, and convection effects are well captured for both wave equations. The computations using Lighthill's equation and AWE-PO are found to provide acoustic intensities within 1.8 dB from the reference direct numerical simulation. This error is comparable with the errors reported for Lighthill's equation in previous studies.**

## I. Introduction

IN MANY industrial applications, an accurate prediction of the sound produced by flow is needed. This requires a deeper understanding of the noise generation mechanisms using proper wave models. The conservation equations of fluid dynamics describe the conversion of flow energy to acoustic energy. This inherent coupling of the flow and acoustics makes a precise investigation of the energy transformation cumbersome. Starting in 1952, Lighthill [1] has looked at the detailed process of converting flow's energy of motion into acoustic energy. This author rearranged the conservation equations into a single wave equation with a right-hand side (RHS), including the sound sources. The RHS of Lighthill's equation is responsible for sound generation, attenuation, convection, refraction, and nonlinear effects. Regarding Lighthill's theory, the sound field is obtained in a sequential procedure [2]. First, a prior direct numerical simulation must be computed to determine the RHS. With this RHS, the sound field can be computed using, for instance, the finite element method (FEM) to solve the wave equation. For specific flows, other wave equations with a different balancing RHS turned out to be useful [3]. For example, Phillips [4] and Lilley [5] noticed that convection effects are part of Lighthill's RHS and moved these convection effects to the wave operator. More recently, Ewert and Schröder [6] derived a set of acoustic perturbation equations based on a method called "source filtering." In their work, several variants are

presented. For instance, one variant focuses on low-Mach-number flows and another has a source term that can be easily computed. For low-Mach-number flows, Seo and Moon [7,8] reformulated the conservation equations, which led to linearized acoustic perturbation equations for low-Mach-number flow with variable density and temperature.

From the linearized Euler equations, Spieser [9] and Spieser and Bailly [10] have derived a scalar wave equation based on the acoustic potential in generalizing the work of Pierce [11]. An aeroacoustic workflow based on this wave equation can be proposed. It is referred to as the aeroacoustic wave equation based on Pierce's operator (AWE-PO) in what follows. Like Lighthill's equation, the noise produced by a flow can be obtained with AWE-PO, using direct numerical simulation (DNS) to calculate the RHS and integrate the wave equation afterward. The first investigations of Pierce's wave operator have shown that it accounts reasonably well for the acoustic propagation over a strongly sheared and heated base flow [12]. The operator has been used to derive an adjoint-based jet noise propagation model [9], and it has been successfully applied to model the installation effects of a subsonic jet beneath a flat plate [13] and noise of a Mach 0.9 jet [14]. In [15], the implementation of the hybrid aeroacoustic workflow using AWE-PO within openCFS [16] was verified and successfully compared with the DNS results of a two-dimensional (2D) mixing layer. The work in hand extends the results of the previous findings. The implementation of AWE-PO uses the developed openCFS algorithms of the perturbed convective wave equation (PCWE) [17], which were successfully applied for human phonation [18–21], fan noise applications [22–24], and heating, ventilation and air conditioning (HVAC) systems [25]. The benefits of the AWE-PO over Lighthill's equation are that it includes the convective effects inside the wave operator instead of having it in the RHS. Referring back to the PCWE and the first investigations on AWE-PO [15], the mesh of the acoustic computation can be coarser than for Lighthill's equation, which allows a faster computation of the acoustic field. On the downside, when using the AWE-PO, an additional step during the RHS computation has to be carried out. Nevertheless, this additional step can be executed for each time step independent of the other time step, allowing parallel and distributed calculations.

The present work aims to investigate the prediction capabilities of the AWE-PO model for noise produced by a high-speed sheared flow. The reliability of the sound prediction is assessed by comparison with

Presented as Paper 2022-2896 at the 28th AIAA/CEAS Aeroacoustics 2022 Conference, Southampton, England, U.K., June 14–17, 2022; received 18 October 2022; revision received 17 April 2023; accepted for publication 24 April 2023; published online Open Access 6 June 2023. Copyright © 2023 by the authors. Published by the American Institute of Aeronautics and Astronautics, Inc., with permission. All requests for copying and permission to reprint should be submitted to CCC at [www.copyright.com](http://www.copyright.com); employ the eISSN 1533-385X to initiate your request. See also AIAA Rights and Permissions [www.aiaa.org/randp](http://www.aiaa.org/randp).

\*Assistant Professor, Institute of Fundamentals and Theory in Electrical Engineering (IGTE), Inffeldgasse 18; also Visiting Scholar at Fluid Mechanics and Acoustics Laboratory (LMFA), Écully, France; [stefan.schoder@tugraz.at](mailto:stefan.schoder@tugraz.at). Member AIAA (Corresponding Author).

<sup>†</sup>Postdoctoral Fellow, Fluid Mechanics and Acoustics Laboratory (LMFA).

<sup>‡</sup>Doctoral Candidate, Fluid Mechanics and Acoustics Laboratory (LMFA).

<sup>§</sup>Full Professor, Fluid Mechanics and Acoustics Laboratory (LMFA). Member Senior AIAA.

the results of Lighthill's equation and the results of a DNS. As in previous studies [26–30], the considered flow is a subsonic mixing layer controlled with a two-frequency excitation so that subsequent vortex pairings produce acoustic waves at a single frequency. The aerodynamic and acoustic fields of the mixing layer are determined using a DNS. The so-obtained flow results are the basis for calculating the respective RHS of both wave equations. Qualitative and quantitative comparisons are made between Lighthill's equation RHS and the AWE-PO RHS. Additionally, the vorticity and the dilatation of the flowfield are visualized. Furthermore, the root-mean-square (RMS) values of the RHS are evaluated along the centerline for additional comparison. Lighthill's wave equation and AWE-PO are used to postprocess the DNS results to obtain the acoustic field using the FEM implemented in openCFS [31]. The acoustic field is subsequently verified and investigated by comparing pressure fluctuation snapshots with the acoustic propagation of DNS. The results and the radiation characteristics of the acoustic intensity are analyzed.

The paper is organized as follows. Section II describes Lighthill's equation and the AWE-PO. In Sec. III, the 2D mixing layer is presented. Section IV reports the numerical methods and the hybrid workflow. The application results are presented in Sec. V. Conclusions are drawn in Sec. VI.

## II. Wave Equations

### A. Lighthill's Wave Equation

Lighthill reformulated the equations of conservation of mass and momentum into a single wave equation. In doing so, a balancing RHS with three terms, namely, the flow velocity contribution, the entropic contribution, and the viscous contribution, was found. The viscous part of the RHS can be omitted in a broad range of applications [32,33]. Also, the entropic contribution was found to be small for an isothermal subsonic Mach 0.9 jet [34] and an isothermal mixing layers [30,35]. Regarding these simplifications of the RHS, Lighthill's wave equation can be written as

$$\left(\frac{1}{c_0^2} \frac{\partial^2}{\partial t^2} - \nabla \cdot \nabla\right) (c_0^2 \rho') = \underbrace{\nabla \cdot \nabla \cdot (\rho \mathbf{u} \otimes \mathbf{u})}_{S_{LH}} \quad (1)$$

where  $\rho' = \rho - \langle \rho \rangle$  is the fluctuating density (with the mean density defined by  $\langle \rho \rangle$  and the instantaneous density  $\rho$ ),  $c_0$  is the ambient speed of sound,  $\mathbf{u}$  is the velocity vector,  $\otimes$  is the dyadic product, and  $S_{LH}$  is the Lighthill RHS. Applying Reynolds decomposition to the velocity  $\mathbf{u} = \langle \mathbf{u} \rangle + \mathbf{u}'$ , with, respectively,  $\langle \mathbf{u} \rangle$  and  $\mathbf{u}'$  the mean velocity and the fluctuating velocity, and by inserting it into the definition of Lighthill's RHS leads to the shear-noise component  $S_{\text{shear}}$  and the self-noise component  $S_{\text{self}}$  [34]:

$$\left(\frac{1}{c_0^2} \frac{\partial^2}{\partial t^2} - \nabla \cdot \nabla\right) (c_0^2 \rho') = \underbrace{\nabla \cdot \nabla \cdot (\rho(\langle \mathbf{u} \rangle \otimes \mathbf{u}' + \mathbf{u}' \otimes \langle \mathbf{u} \rangle))}_{S_{\text{shear}}} + \underbrace{\nabla \cdot \nabla \cdot (\rho(\mathbf{u}' \otimes \mathbf{u}'))}_{S_{\text{self}}} \quad (2)$$

### B. Aeroacoustic Wave Equation Based on Pierce's Operator

Starting from the conservation equations, a convective wave equation can be derived based on the acoustic potential as the dependent variable [9]. The linearized Euler equations can be rewritten as

$$\begin{aligned} D_{(u)}(\rho') + \nabla \cdot (\langle \rho \rangle \mathbf{u}') + \rho' \nabla \cdot \langle \mathbf{u} \rangle &= S_p \\ D_{(u)}(\langle \rho \rangle \mathbf{u}') + (\nabla \langle \mathbf{u} \rangle) \cdot (\langle \rho \rangle \mathbf{u}') + \langle \rho \rangle \mathbf{u}' \nabla \cdot \langle \mathbf{u} \rangle + \nabla p' - \frac{\nabla \langle p \rangle}{\langle \rho \rangle} \rho' &= S_{\rho u} \\ D_{(u)}(p') + \nabla \langle p \rangle \cdot \mathbf{u}' + \langle p \rangle (\nabla \cdot \mathbf{u}') + \gamma p' (\nabla \cdot \langle \mathbf{u} \rangle) &= S_p \end{aligned} \quad (3)$$

with quadratic terms in the fluctuation quantities being the sources derived in [36]:

$$\begin{aligned} S_p &= -\nabla \cdot (\rho' \mathbf{u}') \\ S_{\rho u} &= -\nabla \cdot (\langle \rho \rangle \mathbf{u}' \otimes \mathbf{u}') + \mathbf{u}' (\nabla \cdot (\langle \rho \rangle \mathbf{u}')) + \frac{\nabla p'}{\langle \rho \rangle} \rho' \\ S_p &= -\mathbf{u}' \cdot \nabla p' - \gamma p' \nabla \cdot \mathbf{u}' \end{aligned} \quad (4)$$

where  $D_{(u)} = \partial/\partial t + \langle \mathbf{u} \rangle \cdot \nabla$  is the material derivative based on the mean flow velocity,  $p$  the instantaneous pressure,  $\gamma = c_p/c_v$ ,  $c_p$  is the specific isobaric heat capacity, and  $c_v$  is the specific isochoric heat capacity. The momentum term  $S_{\rho u}$  is manipulated using the vector identities:  $\nabla \cdot (\mathbf{u}' \otimes \mathbf{u}') = (\nabla \mathbf{u}') \cdot \mathbf{u}' + \mathbf{u}' (\nabla \cdot \mathbf{u}')$ ,  $(\mathbf{u}' \otimes \mathbf{u}') \cdot (\nabla \langle \rho \rangle) = \mathbf{u}' (\mathbf{u}' \cdot \nabla \langle \rho \rangle)$ , and  $\nabla \cdot (\langle \rho \rangle \mathbf{T}) = \langle \rho \rangle \nabla \cdot \mathbf{T} + \mathbf{T} \cdot \nabla \langle \rho \rangle$ , with  $\mathbf{T}$  being an arbitrary tensor.

One step further, the fluctuating momentum potential  $\phi$  is defined by the Helmholtz decomposition of the fluctuating momentum:

$$\langle \rho \rangle \mathbf{u}' = \nabla \times \mathbf{A} + \nabla \phi \quad (5)$$

where  $\mathbf{A}$  is the vortical momentum vector potential. Inserting Helmholtz's decomposition into the momentum equation of the linearized Euler equations and using  $\nabla(D_{(u)}\phi) = D_{(u)}(\nabla\phi) + (\nabla\langle\mathbf{u}\rangle)^T \cdot \nabla\phi$  and  $(\nabla \times \langle \mathbf{u} \rangle) \times \nabla \phi = (\nabla \langle \mathbf{u} \rangle) \cdot \nabla \phi - (\nabla \langle \mathbf{u} \rangle)^T \cdot \nabla \phi$  lead to

$$\begin{aligned} \nabla(D_{(u)}\phi + p') + (\nabla \times \langle \mathbf{u} \rangle) \times \nabla \phi + \underbrace{((\nabla \cdot \langle \mathbf{u} \rangle) \nabla \phi - \rho' \nabla \langle p \rangle / \langle \rho \rangle)}_{=0 \text{ for isobaric flows}} \\ + \mathbf{f}(\nabla \times \mathbf{A}) = S_{\rho u} \end{aligned} \quad (6)$$

with  $\mathbf{f}(\nabla \times \mathbf{A}) = D_{(u)}(\nabla \times \mathbf{A}) + (\nabla \cdot \langle \mathbf{u} \rangle)(\nabla \times \mathbf{A}) + (\nabla \langle \mathbf{u} \rangle) \cdot (\nabla \times \mathbf{A})$ . For parallel (isobaric) base flows  $\nabla \langle p \rangle = 0$ , the energy equation  $\langle \mathbf{u} \rangle \cdot \nabla \langle p \rangle + \gamma \langle p \rangle \nabla \cdot \langle \mathbf{u} \rangle = 0$  leads to  $\nabla \cdot \langle \mathbf{u} \rangle = 0$  and one obtains a second-order vectorial partial differential equation for the fluctuating momentum potential [9]. In this linearized framework, governing equations may give rise to instability waves with spatially unbounded growing amplitudes. To guarantee the stability of the propagation model, the vortical mode is discarded in setting  $\nabla \times \mathbf{A} = \mathbf{0}$ . This is acceptable to compute sound propagation [37], but may lead to errors in the acoustic near-field. The term  $(\nabla \times \langle \mathbf{u} \rangle) \times \nabla \phi$  has consistently been discarded in the derivation of AWE-PO. As shown by Yates [38] and Perez Bergliaffa et al. [39], this term is responsible for the coupling between the aerodynamic and the acoustic modes and must be neglected if the vorticity mode is discarded. Assuming that the fluctuating momentum describes potential acoustics leads to  $\langle \rho \rangle \mathbf{u}' = \nabla \phi$  and yields a second-order convective wave operator [11]:

$$D_{(u)}^2 \phi - \nabla \cdot (c_0^2 \nabla \phi) = D_{(u)} S_m = S_{\text{AWE-PO}} \quad (7)$$

with  $S_m$  being the RHS potential that is based on Eq. (10). A detailed discussion on the derivation of the equation can be found in [9]. In the current framework, the fluctuating pressure  $p'$  is defined by the sum of the convective derivative of the potential  $\phi$  and the RHS potential  $S_m$ :

$$p' = -D_{(u)}\phi + S_m \quad (8)$$

This RHS potential  $S_m$  is again based on the Helmholtz decomposition of the self-noise component vector of Eq. (2):

$$\nabla \cdot (\langle \rho \rangle \mathbf{u}' \otimes \mathbf{u}') = \nabla S_m + \nabla \times \mathbf{B} \quad (9)$$

with  $\mathbf{B}$  being the nonradiating vortical potential. The RHS potential of AWE-PO  $S_m$  is computed by Poisson's equation:

$$\nabla \cdot \nabla S_m = \Delta S_m = \nabla \cdot \nabla \cdot (\langle \rho \rangle \mathbf{u}' \otimes \mathbf{u}') \quad (10)$$

In this sense, the self-noise source term is filtered to obtain the radiating RHS potential  $S_m$ . This filtering process isolates the radiating RHS terms from nonradiating structures inside the RHS vector. Maxwell's interpretation of the Laplacian [40] suggests that only the compressible effects inside the source couple effectively into the acoustic field. To sum up, the AWE-PO assumes that the linear effects account for the

acoustic propagation and that the quadratic interactions form the RHS terms. These quadratic interactions correspond to the self-noise component  $S_{\text{self}}$  of Lighthill's RHS in Eq. (2).

### III. Mixing Layer

As in previous studies [26–30,37,41–47], a 2D isothermal mixing layer is considered with the aim of assessing the validity of acoustic wave equations. The flow configuration is similar to those simulated by Colonius et al. [48] and Bogey et al. [49], for instance. The mixing layer is excited at two frequencies  $f$  and  $f/2$ . For illustration, a schematic view of the configuration is shown in Fig. 1. In this figure, vortices and their pairings at a period  $T_p = 2\pi/\omega_p = 2/f$  can be observed at the center of the shear zone. The vortex pairings generate acoustic waves at a frequency  $f/2$  in the acoustic field, as seen in the Fig. 1. They constitute the main sound sources inside the mixing layer. The mixing layer is centered at  $y = 0$ . The velocity  $\mathbf{u} = (u_x, 0)^T$  at the inflow boundary condition is given by the hyperbolic-tangent profile

$$u_x(y) = \frac{U_1 + U_2}{2} - \frac{U_2 - U_1}{2} \tanh\left(\frac{2y}{\delta_\omega}\right) \quad (11)$$

where  $U_1 = 0.3c_0$  and  $U_2 = 0.6c_0$  are the velocities of the slow and rapid flows, respectively, and  $\delta_\omega = (U_2 - U_1)/\max(|du_x/dy|)$  is the vorticity thickness at the upstream boundary, which provides a Reynolds number of  $Re_\omega = \delta_\omega(U_2 - U_1)/\nu = 2000$ , where  $\nu$  is the kinematic viscosity.

### IV. Methods

Figure 2 illustrates how the acoustic field is computed using a hybrid aeroacoustic workflow [2]. Firstly, the flowfield is obtained using a DNS. For Lighthill's formulation, the FEM RHS is computed based on the DNS results. For the AWE-PO, Poisson's equation is solved to obtain the RHS potential  $S_m$ , which is used to compute the FEM RHS. Finally, the sound propagation is simulated.

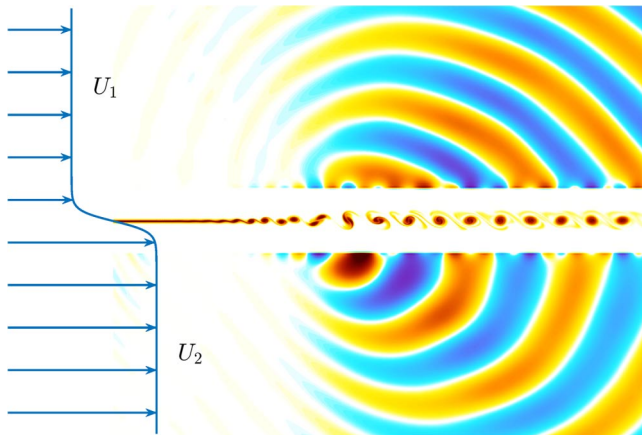


Fig. 1 Schematic view of the mixing layer. Instantaneous vorticity and fluctuating pressure fields are represented at the shear zone's center and periphery.

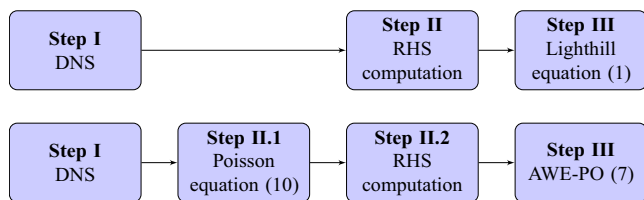


Fig. 2 Schematic of the Lighthill (top) and AWE-PO (bottom) hybrid aeroacoustic workflows to illustrate the computational steps of the methods.

#### A. Step I: Flow Simulation

The DNS of the mixing layer is carried out using an in-house solver to compute the 2D compressible Navier–Stokes equations in Cartesian coordinate  $(x, y)$ , based on low-dissipation and low-dispersion explicit schemes. Fourth-order 11-point centered finite differences are used for spatial discretization, allowing accuracy down to four points per wavelength. A second-order six-stage Runge–Kutta algorithm is implemented for time integration [50]. A sixth-order 11-point centered filter [51] is applied explicitly to the flow variables every time step to remove grid-to-grid oscillations without affecting the waves computed. Noncentered finite differences and filters are also used near the grid boundaries [52]. At the boundaries, the radiation conditions of Tam and Dong [53] are applied, with the addition at the outflow of a sponge zone combining grid stretching and Laplacian filtering [54], to avoid significant acoustic reflections. The DNS is the workflow diagram's first step (flow simulation), as described in Fig. 2.

For the DNS, a domain of dimensions  $L_x/\delta_\omega = 600$  and  $L_y/\delta_\omega = 400$  is used. A nonuniform structured grid discretizes this domain. In the transverse direction, the mesh spacing equals  $\Delta y_0/\delta_\omega = 0.1$  at  $y = 0$ . On both sides of the mixing layer, this mesh spacing is stretched with a rate of 4% until it reaches  $\Delta y/\delta_\omega \approx 2.3$  at  $y/\delta_\omega \approx \pm 55$ . In the axial direction, the mesh spacing equals  $\Delta x_0/\delta_\omega = 0.2$  from  $x/\delta_\omega = 0$  to  $x/\delta_\omega = 250$ . A sponge zone is implemented further downstream, and the mesh spacing is stretched at a rate of 4%. In this sponge zone, the variables are filtered using a Laplacian filter with an intensity growing linearly from zero at  $x/\delta_\omega = 250$  up to 0.2 at  $x/\delta_\omega = 350$ . For  $x/\delta_\omega > 350$ , the intensity is constant and equal to 0.2. The time step size, based on the minimum mesh spacing in the transverse direction and the speed of sound in the ambient medium, is given by  $\Delta t_{\text{DNS}} = \Delta y_0/c_0$ . The mixing layer is excited at its fundamental frequency  $f$ , given by the Strouhal number  $St_\omega = 2f\delta_\omega/(U_2 + U_1) = 0.141$  [55], and at the first sub-harmonic  $f/2$ . This excitation allows the formation of vortices at a fixed position  $x/\delta_\omega \approx 70$  and the occurrence of vortex pairings at  $x/\delta_\omega \approx 110$ . Each vortex pairing period is discretized by  $T_p/\Delta t_{\text{DNS}} = 315$ , and after  $500T_p$  the data at every third time step are stored for the computation of Lighthill's RHS term (1) and the AWE-PO RHS term (10). A duration of  $50T_p$  is computed and exported for this investigation.

#### B. Step II: RHS Computation

Regarding best practice for hybrid aeroacoustics RHS computations using FEM [56,57], the RHS of Lighthill (1) and AWE-PO (7) were computed on the DNS grid and conservatively integrated to the acoustic mesh [24]. The conservative integration was carried out by the cell-centered method [23].

##### 1. Lighthill's Wave Equation

The RHS  $S_{\text{LH}}$  of Lighthill's wave equation (1) is computed using the DNS solution. The mean part of the Lighthill RHS  $\langle S_{\text{LH}} \rangle$  is eliminated according to [49]. The RHS computation is the second step of the workflow diagram of Lighthill's equation, described in Fig. 2.

##### 2. Aeroacoustic Wave Equation Based on Pierce's Operator

Poisson's equation (10) was solved using the open-source FEM simulation software openCFS [16] method *acousticSplitPDE* with the option *scalar* to compute the scalar part of the Helmholtz decomposition [58–60]. The computational domain coincides with the 2D flow domain and uses finite element nodes located at the finite difference point coordinates. Linear quadrilateral Lagrangian finite elements are used. An infinite mapping layer surrounds this domain and uses the 2D free-field characteristics to account for the elliptic free-field [61] with a homogeneous Dirichlet boundary at infinity. Each time step can be calculated individually, decreasing the duration of this workflow step significantly with parallel processes. Based on Poisson's equation (10), the RHS potential  $S_m$  is calculated. Subsequently, the AWE-PO RHS  $S_{\text{AWE-PO}}$  is computed by the material derivative [18]. Together, the calculation of Poisson's equation (10) (substep II.1) and the subsequent AWE-PO RHS computation

(substep II.2) form the second step of the workflow diagram of the AWE-PO, described in Fig. 2.

### C. Step III: Acoustic Simulation

Lighthill's equation (1) and AWE-PO (7) are solved using the openCFS [16] method *acousticPDE* with linear quadrilateral Lagrangian finite elements. The computational domain has the dimensions of the flow domain. The mesh uses a uniform discretization of  $\Delta x/\delta_\omega \approx 0.17$  and  $\Delta y/\delta_\omega \approx 0.35$ . A perfectly matched layer (PML) with an inverse damping function region surrounds the mesh to reduce boundary reflections [62]. The PML uses the same discretization, with four layers of elements toward the free-field direction. The grid resolution and the number of elements toward the free-field direction were studied to ensure an accurate resolution of the wave equations. The used PML implementation does not account for a background flowfield.

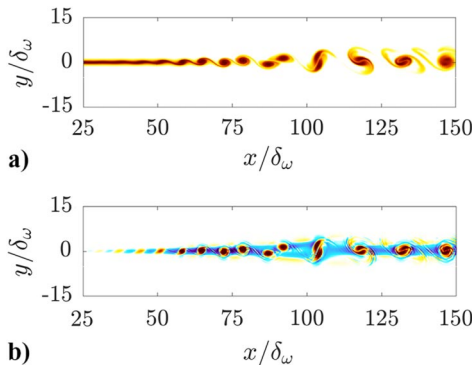
The material derivatives appearing in the AWE-PO have been computed considering the mean flow velocity  $\langle \mathbf{u} \rangle$ . The AWE-PO is solved with a stable convective wave formulation [31]. A systematic mesh study was performed to guarantee a sufficient accurate resolution, relying on the rules of Ainsworth [63]. The time step size was chosen according to the DNS result data time steps  $\Delta t_{CA} = 3\Delta t_{DNS}$ , and the acoustic field was initialized with zeros homogeneously. For Lighthill's equation and the AWE-PO, the amplitude of the RHS term was gradually introduced temporally. Spatially, the RHS term was truncated smoothly over two wavelengths to minimize the truncation effects [64]. The dispersion-controlled Hilber–Hughes–Taylor scheme performs time stepping [65]. The acoustic simulation is the third and final step of the workflow diagrams, described in Fig. 2.

## V. Results

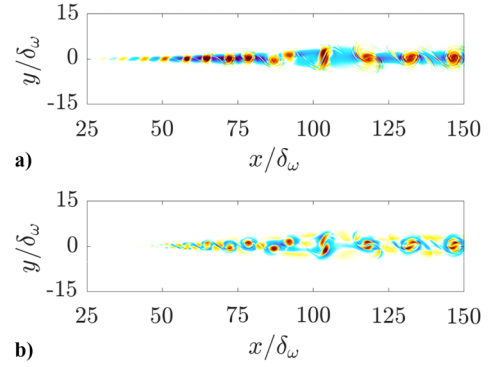
### A. Snapshots of the Source Terms

Figure 3 shows the vorticity of the flowfield and Lighthill's RHS values  $S_{LH}$ . Regarding the vorticity in Fig. 3a, a laminar shear layer can be observed in the region  $x/\delta_\omega < 50$ . It starts to roll-up until the vortex merges at  $x/\delta_\omega \approx 110$ . During the pairing, the appearance of the vorticity structures changes compared to the roll-up. Further downstream, larger vortices, having about twice the diameter of the vortices in the roll-up at  $x/\delta_\omega \approx 75$ , are found. The locations of the vortices during the roll-up of the mixing layer and the merging are referred to in the discussion of the RHS terms of the wave equations. Turning to Fig. 3b and the region  $x/\delta_\omega < 50$ , the Lighthill's RHS values are small relative to the RHS values for  $x/\delta_\omega > 50$ . Between  $x/\delta_\omega \approx 50$  and  $x/\delta_\omega \approx 90$ , the consecutive vortices, marked by red regions in the RHS, start to influence each other. At the pairing location around  $x/\delta_\omega \approx 110$ , the colored pattern of the Lighthill RHS term looks different from the one during the roll-up of the mixing layer. Between the vortices, the RHS values are visible in blue, indicating an opposite sign. In [45], correlations between this Lighthill RHS and the vortical structures in terms of the vorticity were drawn.

Snapshots of Lighthill's shear-noise term  $S_{shear}$  and self-noise term  $S_{self}$  are provided in Figs. 4a and 4b, respectively. Focusing on Fig. 4a



**Fig. 3** Snapshots of a) the vorticity  $\omega_z/(\Delta U/\delta_\omega)$  and b) Lighthill's RHS term  $SLH/(\rho_0\Delta U^2/\delta_\omega^2)$ , where  $\rho_0 = 1.19\text{kg/m}^3$  is the density of the surrounding fluid and  $\Delta U = U_2 - U_1$ . The color scales range between  $\pm 0.2$  for the RHS and between  $\pm 1$  for vorticity, from blue to red.



**Fig. 4** Snapshots of a) the shear-noise part of Lighthill's RHS  $S_{shear}/(\rho_0\Delta U^2/\delta_\omega^2)$  and b) self-noise part of Lighthill's RHS  $S_{self}/(\rho_0\Delta U^2/\delta_\omega^2)$ . The color scales range between  $\pm 0.2$  from blue to red.

and the region  $x/\delta_\omega < 50$ , the RHS values are small and are similar to Lighthill's RHS values. During the shear layer roll-up, the shear-noise terms have a color pattern like Lighthill's RHS. At the pairing, their appearance changes from circular red structures at the vortex positions to two elongated red regions as a result of the merging. Right before the pairing location, the values of shear-noise terms are smaller than Lighthill's RHS values, since the self-noise interaction becomes significant in this region. In Fig. 4b, no self-noise part is visible in regions upstream of  $x/\delta_\omega \approx 50$ . As the  $x$  coordinate approaches the pairing location, the self-noise term grows significantly and changes its shape during vortex pairing. Each vortical red structure is encircled by a blue ring. Between two consecutive vortices, the RHS magnitude is low. This self-noise part of Lighthill's RHS term  $S_{self}$  is the RHS of Poisson's equation of the AWE-PO (10). Compared to Lighthill's RHS values, the magnitude is concentrated at the location of the pairings. In the next step, the RHS values of Fig. 4 are discussed at the pairing location. The shear-noise part consists of two red structures indicating the two vortices that are subject to merging. In the snapshot of the shear-noise part, the RHS values representing the two vortices are separated by a thin inclined blue line at  $x/\delta_\omega \approx 105$ . In contrast to that, the self-noise part structure turns first from blue to red and then again from red to a blue region. The two red regions in the center of the self-noise part at the pairing location are again separated by an inclined blue line.

Figure 5 shows the AWE-PO RHS potential  $S_m$ , the material derivative of the RHS potential  $S_m$ , defining the RHS of AWE-PO

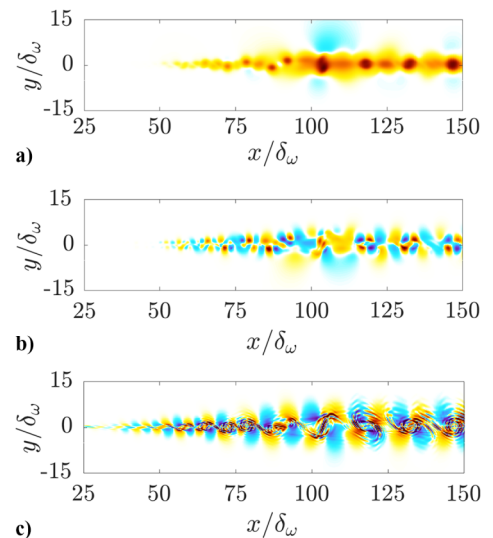


**Fig. 5** Snapshots of a) the AWE-PO RHS potential  $S_m/(\rho_0\Delta U^2)$ , b) the RHS of AWE-PO  $S_{AWE-PO}/(\rho_0\omega_p^2\Delta U^2/c_0^2)$ , and c) fluid dilatation  $\nabla \cdot \mathbf{u}/(\Delta U/\delta_\omega)$ . The color scales range between  $\pm 0.02$  for subfigures (a) and (b), and between  $\pm 0.005$  for the dilatation shown in subfigure (c), from blue to red.

(7), and the fluid dilatation  $\nabla \cdot \mathbf{u}$ . Regarding the filtered RHS  $S_m$  in Fig. 5a, source levels are highest at the vortex location. At the pairings, the high values of the RHS potential result in a large red structure. Focusing on the RHS of AWE-PO in Fig. 5b, the overall shape differs from the previously discussed Lighthill's RHS. The most important difference is discussed based on looking at a single vortex at  $x/\delta_\omega \approx 75$ . At this location, the Lighthill's source term values are represented by a red region, whereas the AWE-PO RHS values are represented by a cluster of red and blue regions. From the AWE-PO RHS, it is not obvious where the vortices are located, making AWE-PO RHS difficult to interpret. Similar to the self-noise part, the RHS of AWE-PO is not visible for  $x/\delta_\omega < 50$ . During the roll-up, the AWE-PO RHS values increase until the pairing. At the pairing  $x/\delta_\omega \approx 110$ , a pair of two red regions, surrounded by alternating red and blue structures, is found. After the pairing location, the RHS term looks like convected structures with a quadrupolar shape. If the filtered source  $S_m$  was simply convected downstream of the vortex pairing, it would have completely been filtered out by the material derivative that applies to it. The presence of this quadrupole-like pattern is interpreted as an effect of the flow shearing. This distribution of AWE-PO's RHS (see Fig. 5b) is substantially different from the shape of the self-noise RHS (see Fig. 4b), but is closely similar to the dilatation field  $\nabla \cdot \mathbf{u}$  presented in Fig. 5c. Close to  $x/\delta_\omega \approx 150$ , the self-noise part features elongated red elliptical shapes surrounded by a blue ring, while the AWE-PO RHS is a cluster of four alternating red and blue regions. In Fig. 5c, the dilatation structures grow in magnitude and size during the roll-up. Smooth blue and red dilatation structures are located in the regions where the AWE-PO RHS has circular blue or red regions. These structures extend into the  $y$  direction. They have the same quadrupolar shape as the AWE-PO source. This suggests that the sound source of the AWE-PO built from Lighthill's stress tensor is consistent with the sound sources originating from the dilatation of the fluid [66].

The source terms in Figs. 3 and 5 differ in shape and magnitude. The amplitude of Lighthill's source is significant all along the shear layer, as observed by Colonius et al. [48] in their study of Lilley's acoustic analogy. This high magnitude can be explained by the definition of the Lamb vector  $(\nabla \times \mathbf{u}') \times \mathbf{u}'$  being one major part of the Lighthill's source and having a high value in sheared fluid zones. The amplitude of the source terms in the AWE-PO is smaller than those in the Lighthill's equation RHS in Fig. 3, and than those of the shear-noise term and the self-noise term in Fig. 4. This results in an overall source amplitude of about one order of magnitude smaller in the AWE-PO case.

## B. Discussion of AWE-PO Source Term

The section discusses the source term of Fig. 5 in more detail. The individual source term parts of the material derivative are split as follows:

$$S_{\text{AWE-PO}} = \underbrace{\frac{\partial S_m}{\partial t}}_{S_{m,t}} + \underbrace{\langle \mathbf{u} \rangle \cdot \nabla S_m}_{S_{m,\text{conv}}} \quad (12)$$

Figure 6 shows the RMS values of the Lighthill RHS  $S_{\text{LH,rms}}$ , of the AWE-PO RHS  $S_{\text{AWE-PO,rms}}$ , of the partial time derivative part of AWE-PO RHS  $S_{\text{AWE-PO,t,rms}}$ , and of the convective derivative part of the AWE-PO RHS  $S_{\text{AWE-PO,conv,rms}}$  along the mixing layer centerline. The RMS values of the Lighthill RHS term are higher than those of the other RHS terms. In contrast, the RMS values of the partial time derivative part  $S_{\text{AWE-PO,t,rms}}$  and the RMS of the convective derivative part of the AWE-PO RHS  $S_{\text{AWE-PO,conv,rms}}$  are of similar magnitude. The RMS values of the AWE-PO RHS term  $S_{\text{AWE-PO,rms}}$  are about one order of magnitude smaller than those of the other ones. The partial time derivative is compensated for a large part by the convective derivative part of the RHS of AWE-PO as indicated by [33]. This substantial reduction of the source magnitude is referred to as the filtering property of the material derivative, which filters frozen flow structures  $S_m^f$ . The RHS of the AWE-PO can be split into a frozen part  $S_m^f(\xi)$  with  $\xi(t) = \mathbf{x} - U\mathbf{t}$  and a remaining part  $S_m^*(\mathbf{x}, t)$ :

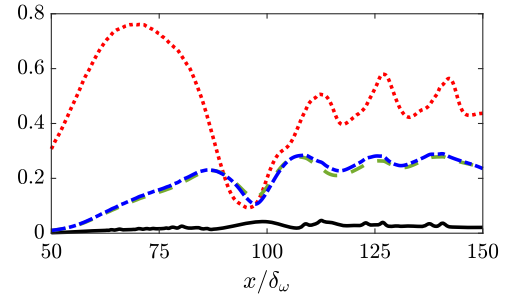


**Fig. 6** Normalized root-mean-square RHS values at ( $y = 0$ ) inside the mixing layer. Lighthill's RHS is normalized by  $0.02\rho_0 c_0^2/\delta_\omega^2$  and the AWE-PO RHS by  $0.02\rho_0 c_0^2\omega_p$ ; —, AWE-PO RHS  $S_{\text{AWE-PO,rms}}$ ; — —, AWE-PO  $S_{\text{AWE-PO,t,rms}}$ ; - - - , AWE-PO  $S_{\text{AWE-PO,conv,rms}}$ ; ····, Lighthill's RHS  $S_{\text{LH,rms}}$ .

$$S_m(\mathbf{x}, t) = S_m^f + S_m^*(\mathbf{x}, t) \quad (13)$$

The frozen part satisfies Taylor's hypothesis [67] and hence vanishes when calculating the material derivative

$$\frac{DS_m^f(\xi)}{Dt} = 0 \quad (14)$$

Therefore in the case of vortical structures, which are convected in a nearly frozen manner, the source term  $S_m$  is subject to a strong filtering and consequently the source magnitude is reduced.

As a result, the RHS of AWE-PO contains only nonfrozen source structures. A similar RHS term reduction has been found in three-dimensional (3D) for the PCWE but has not been explained yet [18,22]. All source contributions removed by the material derivative in the AWE-PO's source term are not efficiently converted into sound emission considering a subsonic flow and do not radiate.

## C. Acoustic Solution

The acoustic radiations obtained by the DNS, Lighthill's equation, and the AWE-PO are compared against each other. The fluctuating pressure of Lighthill's equation is defined by  $p' = c_0^2 \rho'$  [30] and the one for AWE-PO is calculated by Eq. (8).

Figure 7 shows the pressure fluctuations  $p'$  obtained by the DNS, Lighthill's wave equation, and the AWE-PO. The DNS result exhibits acoustic waves convected by the base flow. This convective effect is substantial in the lower rapid flow section. Wave amplitudes are larger in the flow direction than in the upstream direction. The pressure fluctuations inside the mixing layer are of several orders of magnitude higher than the ones in the periphery and similar to the ones obtained in [35]. The DNS result serves as a reference in what follows. Focusing on the results from Lighthill's equation, the radiation pattern is similar to that from the DNS results. Low-amplitude oscillations are found in the fluctuating pressure field in the upstream direction, both above and below the mixing layer. A mesh convergence study has been conducted to verify that these oscillations are not due to insufficient mesh refinement. Above the mixing layer and downstream of the pairing, the results of Lighthill's equation slightly deviate from the DNS in a polar region of  $\theta = \pm 15^\circ$ , with the polar angle  $\theta$  counted in the counterclockwise direction from the downstream flow region and the origin of the polar coordinate system at the pairing location. The deviations increase close to the mixing layer for  $x/\delta_\omega > 150$ . The pressure fluctuations inside the sheared flow have a similar pattern as the results from the DNS. This agreement is expected since Lighthill's equation is an exact reformulation of the conservation equations and recovers the fluctuating pressure.

Regarding the results from the AWE-PO, the radiation pattern is in good accordance with the DNS results and the results of Lighthill's equation. As for the results computed from Lighthill's equation, minor deviations occur in the upstream region for  $x/\delta_\omega < 100$ . Downstream of the pairing location, the fluctuating pressure field in the slow flow region has an extinction line at  $\theta = 15^\circ$ . A similar

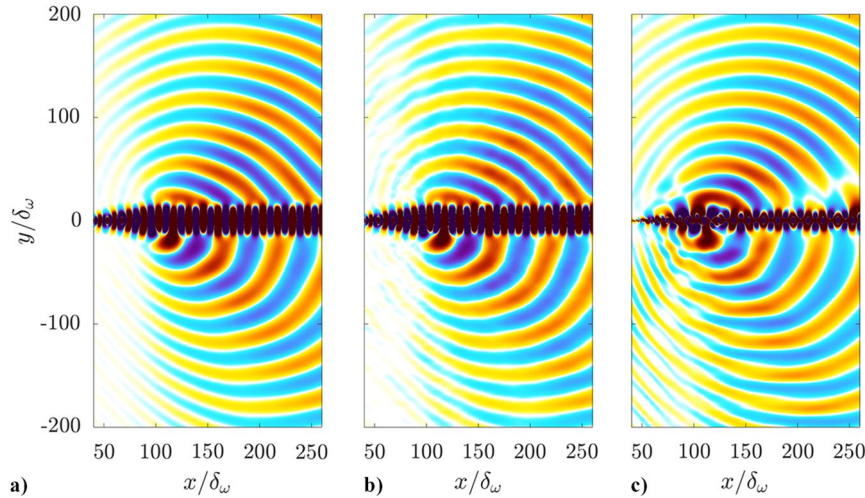


**Fig. 7** Fluctuating pressure fields  $p' / (\rho_0 c_0^2)$  from a) DNS, b) Lighthill's equation (1), and c) AWE-PO (5). The plots use a color scale minimum and maximum values of  $\pm 1.5 \cdot 10^{-4}$ , from blue to red.

extinction line was found in [35] and has been associated with insufficient integration over the source region regarding the  $x$  direction. The integration over the source region was examined in the present study and was not found to be responsible for this line. When deriving the wave equation, the vortical mode is neglected, which is a possible reason for the reduction of the fluctuating pressure at  $\theta = 15^\circ$ . The oscillations in the upstream results of the AWE-PO are attributed to the PML used, which does not account for a background flow. The amplitudes of the reflections arising at the boundary conditions are stronger in the rapid flow region ( $y < 0$ ) than in the slow flow region, which supports this explanation of the oscillations based on the PML. On the lower side, the radiation characteristics and the convective effects for this  $M = 0.6$  region are predicted well for the AWE-PO, with a slight overprediction of the upstream radiation.

Figure 8 shows the acoustic intensity

$$L_I = 10 \log \frac{I}{I_0} \quad (15)$$

where  $I = \langle p'^2 \rangle / (\rho_0 c_0)$  and  $I_0 = 10^{-12} \text{ W} \cdot \text{m}^{-2}$  is used. The directivities are evaluated over circles of radius  $r/\delta_\omega = 120$  centered on the vortex pairing location, from  $\theta = 10^\circ$  to  $\theta = 90^\circ$  in the upper flow, and from  $\theta = -90^\circ$  to  $\theta = -10^\circ$  in the lower flow. The acoustic intensities obtained from the three methods agree fairly well below the mixing layer. The DNS results predict the main lobe at an angle of  $\theta = -45^\circ$ , while the main lobe is predicted closer to the mixing layer at  $\theta = -55^\circ$  for the AWE-PO and the results of Lighthill's equation

reach a plateau between  $\theta = -45^\circ$  and  $\theta = -15^\circ$ . The acoustic intensity from Lighthill's equation matches the DNS result very well, with a maximum deviation of less than 0.2 dB. Minor deviations occur for the AWE-PO results compared to the DNS in this region, with a maximum deviation at an angle of  $\theta = -90^\circ$  of about 0.5 dB. Above  $\theta = -45^\circ$ , the acoustic intensity results of the AWE-PO deviate by less than 0.2 dB from the DNS results. These slight deviations are comparable to those obtained previously in [35], where the maximum deviation using the full Lighthill RHS [68] was less than 1 dB. Again, the acoustic intensities agree fairly well above the mixing layer for  $\theta > 30^\circ$ . There is no main lobe visible for the DNS results, nor for the results obtained with Lighthill's formulation. There is a slight reduction of the acoustic intensity obtained with Lighthill's equation compared to the DNS at  $\theta = 15^\circ$ . The AWE-PO predicts the main lobe at  $\theta = 40^\circ$ . Above  $\theta = 45^\circ$ , the acoustic intensities of the wave equations match the DNS results very well, with a maximum deviation of less than 0.3 dB. Lighthill's equation deviates from the DNS results by less than 0.3 dB. For the AWE-PO, an intensity reduction is visible at  $\theta = 15^\circ$ . However, the maximum deviation of 1.8 dB is comparable to those obtained previously in [35].

As a next step, the self-noise and shear-noise contributions of Lighthill's equation (1) are investigated in detail. Figure 9 shows the self-noise and shear-noise contributions to the fluctuating pressure and the result of the full Lighthill equation (1). Turning to the fluctuating pressure of the self-noise component  $S_{\text{self}}$ , between  $\theta = \pm 70^\circ$ , Fig. 9a shows higher wave amplitudes than those of

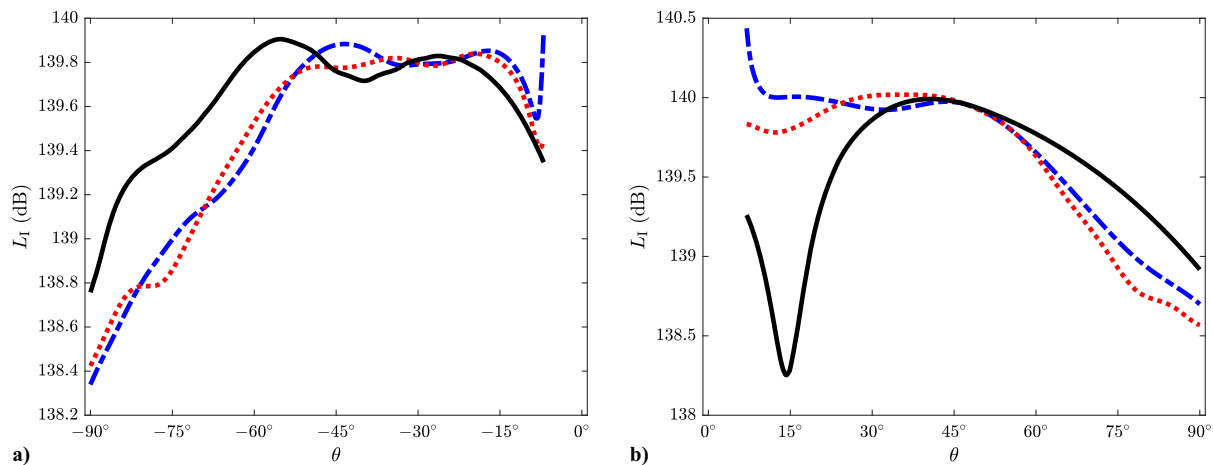


**Fig. 8** Acoustic intensity  $L_I$  depending on the angle  $\theta$  a) in the rapid flow below the mixing layer and b) in the slow flow region above the mixing layer: ---, DNS; ···, Lighthill's equation; —, AWE-PO.

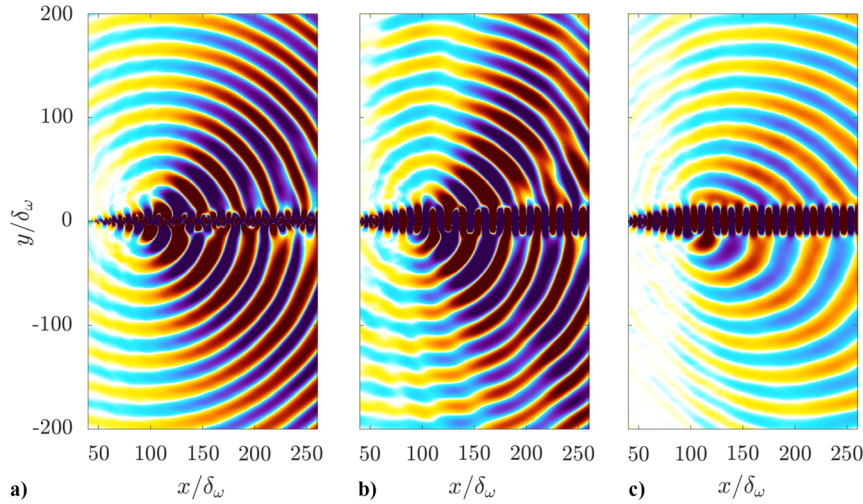


**Fig. 9** Fluctuating pressure fields  $p' / (\rho_0 c_0^2)$  from a) the self-noise contribution, b) the shear-noise contribution, and c) the full Lighthill RHS term. The plots use a color scale minimum and maximum values of  $\pm 1.5 \cdot 10^{-4}$ , from blue to red.

Fig. 9c. The radiation lobe points toward  $\theta = 60^\circ$  above the mixing layer and is slightly lower for the lobe below the mixing layer in the rapid flow region. Overall, no wave convection effects are observable for the fluctuating pressure field  $p'$  using the self-noise component. Figure 9b shows the fluctuating pressure of the shear-noise component  $S_{\text{shear}}$ . The wavefronts above and below the mixing layer are not circular. Starting at a location inside the mixing layer at  $x/\delta_\omega \approx 200$ , the shape of the wavefronts depends on the angle  $\theta$ . At around  $\theta = 90^\circ$ , the wavefront has an angular discontinuity. Below the mixing layer, there are several angles (namely, at about  $\theta = -80^\circ$ ,  $\theta = -85^\circ$ , and  $\theta = -90^\circ$ ) of angular discontinuities. Figure 9c shows the fluctuating pressure as a result of using the full Lighthill's RHS term. Interestingly, both the fluctuating pressure of self-noise and shear-noise term have higher wave amplitudes than the ones of the full Lighthill equation. The self-noise and shear-noise RHS terms compensate for each other to accurately predict emissions and convection effects. This effect was found previously in [69].

The radiated fields obtained from the partial time derivative part  $S_{\text{AWE-PO},t}$ , from the convective derivative part  $S_{\text{AWE-PO},\text{conv}}$  only, and from the full AWE-PO equation (7) are shown in Figs. 10a–10c, respectively. In Fig. 10a, the radiation pattern is very similar to the radiation pattern from the full AWE-PO RHS term  $S_{\text{AWE-PO}}$ . Minor oscillations and a reduction at  $\theta = 15^\circ$  compared with the main lobe are visible. The fluctuating pressure at the main lobe is higher than for the full AWE-PO results in Fig. 10c. In Fig. 10b, the pressure field

based on the convective derivative part  $S_{\text{AWE-PO},\text{conv}}$  is unexpectedly small and only significant in a range of  $\theta = \pm 30^\circ$ . Interestingly, the waves shape above the mixing layer is inclined like the waves of the DNS at this location. Furthermore, the pressure fluctuations in Fig. 10b are in the opposite phase to the one in Fig. 10a. A substantial reduction in the magnitude of the AWE-PO RHS values was observed in Sec. V.B and attributed to the filtering property of the material derivative. In contrast to that, the fluctuating pressure field results indicate that only the time derivative part of the AWE-PO equation  $S_{\text{AWE-PO},t}$  contributes effectively to the radiated pressure field. Inside the sheared flow, the pressure fluctuations of the AWE-PO is low compared to the ones of the DNS and Lighthill's equation.

## VI. Conclusions

A convective wave equation based on Pierce's operator is applied to a 2D mixing layer using a three-step workflow to predict the sound field. Firstly, the flowfield of the mixing layer is obtained by a DNS. Based on this DNS result, the aeroacoustic sources are computed. Finally, the wave equations are solved numerically to predict the mixing layer sound.

Snapshots of the AWE-PO RHS term are compared with Lighthill's RHS, the shear-noise part of Lighthill's RHS, and the self-noise part of Lighthill's RHS. The shape and amplitude of the AWE-PO RHS significantly differ from the RHS values obtained by Lighthill's

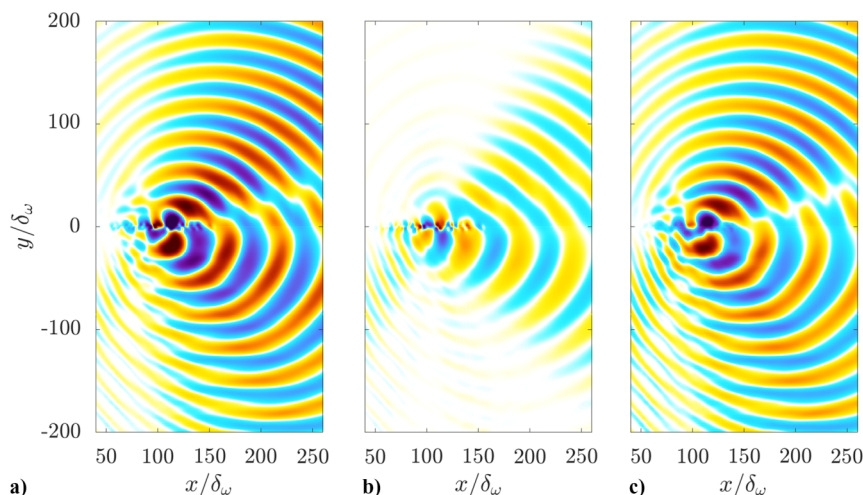


**Fig. 10** Fluctuating pressure fields  $-D_{(w)}\phi / (\rho_0 c_0^2)$  obtained a) from the partial time derivative part of the AWE-PO (5) source as RHS, b) from the convective derivative part of the AWE-PO (5) source as RHS, and c) from the full AWE-PO (5). The plots use a color scale minimum and maximum values of  $\pm 1.5 \cdot 10^{-4}$ .

equation. Lighthill's RHS contains the acoustic source and the necessary convection effects for correct sound propagation. During the derivation of the AWE-PO, the convection effect is shifted to the wave operator. In doing so, the RHS term of the AWE-PO is computed by the material derivative of a source potential obtained by solving a Poisson equation with Lighthill's self-noise term as RHS. The magnitude of AWE-PO RHS is 90% lower than Lighthill's one. The material derivative that applies to the source potential  $S_m$  is responsible for this magnitude reduction. In contrast to Lighthill's RHS term, the AWE-PO RHS values show clusters of four alternating positive and negative source values at the locations of a vortex. These clusters look like a quadrupole in the region of steady vortex convection after the pairing.

The pressure fluctuations obtained from the AWE-PO are compared with those of Lighthill's equation and the reference DNS. Lighthill's equation and the AWE-PO reasonably account for the acoustic propagation. A quantitative comparison of the acoustic intensity of the DNS with Lighthill's equation and the AWE-PO show errors of less than 0.3 and 1.8 dB, respectively. This error range is comparable to the ones reported for Lighthill's equation in other studies [35]. The convection effects of the wavefronts are predicted well for the wave equations. At an angle of  $\theta = 15^\circ$ , the AWE-PO pressure fluctuations are reduced by nearly 1.8 dB. The origin of this line at  $\theta = 15^\circ$  is not clear yet. Furthermore, the effects of the individual terms of the material derivative (the partial time derivative and the convective derivative) are investigated. In contrast to the magnitude reduction inside the source term, the pressure fluctuations when only using the partial time derivative term of the AWE-PO source are in fair agreement with the one obtained using the full AWE-PO RHS term. To conclude, the findings support the ability of the presented AWE-PO to predict mixing layer sound, with far-field acoustic results agreeing with DNS results.

### Acknowledgments

We acknowledge the authors of openCFS. The first author received support from the FFG, TU Graz Mobility, and the Erasmus+ funding, and was supported by TU Graz Open Access Publishing Fund. The second author received support from the AMBROSIA project, founded by The French Civil Aviation Authority (DGAC Convention 2019-18). The third author was supported by the FUI25 Ciblage des sources par voie Logicielle et Méthodes inverses pour l'AéroAcoustique (CALM-AA) regional project, cofinanced by the European regional development fund. This work was granted access to the HPC resources of Pôle de Modélisation et de Calcul en Sciences de l'Ingénieur de l'Information (PMCS2I) of École Centrale de Lyon. It was performed within the framework of the LABEX CeLya (ANR-10-LABX-0060) of Université de Lyon, within the program *Investissements d'Avenir* (ANR-16-IDEX-0005) operated by the French National Research Agency (ANR).

### References

- [1] Lighthill, M., "On Sound Generated Aerodynamically I: General Theory," *Proceedings of the Royal Society of London*, Vol. 211, No. 1107, 1952, pp. 564–587. <https://doi.org/10.1098/rspa.1952.0060>
- [2] Schoder, S., and Kaltenbacher, M., "Hybrid Aeroacoustic Computations: State of Art and New Achievements," *Journal of Theoretical and Computational Acoustics*, Vol. 27, No. 4, 2019, Paper 1950020. <https://doi.org/10.1142/S2591728519500208>
- [3] Schoder, S., Weitz, M., Maurerlehner, P., Hauser, A., Falk, S., Kniesburges, S., Döllinger, M., and Kaltenbacher, M., "Hybrid Aeroacoustic Approach for the Efficient Numerical Simulation of Human Phonation," *Journal of the Acoustical Society of America*, Vol. 147, No. 2, 2020, pp. 1179–1194. <https://doi.org/10.1121/10.0000785>
- [4] Phillips, O. M., "On the Generation of Sound by Supersonic Turbulent Shear Layers," *Journal of Fluid Mechanics*, Vol. 9, No. 1, 1960, pp. 1–18. <https://doi.org/10.1017/S0022112060000888>
- [5] Lilley, G. M., "On the Noise from Jets," AGARD CP-131, 1974.
- [6] Ewert, R., and Schröder, W., "Acoustic Perturbation Equations Based on Flow Decomposition via Source Filtering," *Journal of Computational Physics*, Vol. 188, No. 2, 2003, pp. 365–398. [https://doi.org/10.1016/S0021-9991\(03\)00168-2](https://doi.org/10.1016/S0021-9991(03)00168-2)
- [7] Seo, J., and Moon, Y., "Perturbed Compressible Equations for Aeroacoustic Noise Prediction at Low Mach Numbers," *AIAA Journal*, Vol. 43, No. 8, 2005, pp. 1716–1724. <https://doi.org/10.2514/1.3001>
- [8] Seo, J. H., and Moon, Y. J., "Linearized Perturbed Compressible Equations for Low Mach Number Aeroacoustics," *Journal of Computational Physics*, Vol. 218, No. 2, 2006, pp. 702–719. <https://doi.org/10.1016/j.jcp.2006.03.003>
- [9] Spieser, É., "Adjoint-Based Jet Noise Propagation Model for the Acoustic Potential," Ph.D. Thesis, École Centrale de Lyon, Laboratoire de Mécanique des Fluides et d'Acoustique (LMFA)—CIFRE Safran Aircraft Engines, N° 2020LYSEC43, Écully, France, 2020, [https://acoustique.ec-lyon.fr/publi/spieser\\_thesis.pdf](https://acoustique.ec-lyon.fr/publi/spieser_thesis.pdf).
- [10] Spieser, É., and Bailly, C., "L'équation de Pierce et ses lois de Conservation," *25th Congrès Français de Mécanique (CFM)*, Association Française de Mécanique (AFM), 2022.
- [11] Pierce, A. D., "Wave Equation for Sound in Fluids with Unsteady Inhomogeneous Flow," *Journal of the Acoustical Society of America*, Vol. 87, No. 6, 1990, pp. 2292–2299. <https://doi.org/10.1121/1.399073>
- [12] Spieser, É., and Bailly, C., "Sound Propagation Using an Adjoint-Based Method," *Journal of Fluid Mechanics*, Vol. 900, Oct. 2020, p. A5. <https://doi.org/10.1017/jfm.2020.469>
- [13] Spieser, É., Legendre, C., and Bailly, C., "Acoustic Modelling of the Installation Effects of a Subsonic Jet Beneath a Flat Plate," *28th AIAA/CEAS Aeroacoustics 2022 Conference*, AIAA Paper 2022-2858, 2022. <https://doi.org/10.2514/6.2022-2858>
- [14] Spieser, É., Bogey, C., and Bailly, C., "Noise Predictions of a Mach 0.9 Round Jet Using Tailored Adjoint Green's Functions," *Journal of Sound and Vibration*, Vol. 548, March 2023, Paper 117532. <https://doi.org/10.1016/j.jsv.2022.117532>
- [15] Schoder, S., Kaltenbacher, M., Spieser, É., Vincent, H., Bogey, C., and Bailly, C., "Aeroacoustic Wave Equation Based on Pierce's Operator Applied to the Sound Generated by a Mixing Layer," *28th AIAA/CEAS Aeroacoustics 2022 Conference*, AIAA Paper 2022-2896, 2022. <https://doi.org/10.2514/6.2022-2896>
- [16] Schoder, S., and Roppert, K., "openCFS: Open Source Finite Element Software for Coupled Field Simulation—Part Acoustics," arXiv Preprint, arXiv:2207.04443, 2022. <https://doi.org/10.48550/arXiv.2207.04443>
- [17] Kaltenbacher, M., Hüppe, A., Reppenhagen, A., Zenger, F., and Becker, S., "Computational Aeroacoustics for Rotating Systems with Application to an Axial Fan," *AIAA Journal*, Vol. 55, No. 11, 2017, pp. 3831–3838. <https://doi.org/10.2514/1.J055931>
- [18] Schoder, S., Maurerlehner, P., Wurzing, A., Hauser, A., Falk, S., Kniesburges, S., Döllinger, M., and Kaltenbacher, M., "Aeroacoustic Sound Source Characterization of the Human Voice Production—Perturbed Convective Wave Equation," *Applied Sciences*, Vol. 11, No. 6, 2021, p. 2614. <https://doi.org/10.3390/app11062614>
- [19] Falk, S., Kniesburges, S., Schoder, S., Jakubaß, B., Maurerlehner, P., Echternach, M., Kaltenbacher, M., and Döllinger, M., "3D-FV-FE Aeroacoustic Larynx Model for Investigation of Functional Based Voice Disorders," *Frontiers in Physiology*, Vol. 12, March 2021, p. 226. <https://doi.org/10.3389/fphys.2021.616985>
- [20] Lasota, M., Šidlof, P., Kaltenbacher, M., and Schoder, S., "Impact of the Sub-Grid Scale Turbulence Model in Aeroacoustic Simulation of Human Voice," *Applied Sciences*, Vol. 11, No. 4, 2021, p. 1970. <https://doi.org/10.3390/app11041970>
- [21] Valášek, J., Kaltenbacher, M., and Sváček, P., "On the Application of Acoustic Analogies in the Numerical Simulation of Human Phonation Process," *Flow, Turbulence and Combustion*, Vol. 102, No. 1, 2019, pp. 129–143. <https://doi.org/10.1007/s10494-018-9900-z>
- [22] Schoder, S., Junger, C., and Kaltenbacher, M., "Computational Aeroacoustics of the EAA Benchmark Case of an Axial Fan," *Acta Acustica*, Vol. 4, No. 5, 2020, p. 22. <https://doi.org/10.1051/aacus/2020021>
- [23] Schoder, S., Wurzing, A., Junger, C., Weitz, M., Freidhager, C., Roppert, K., and Kaltenbacher, M., "Application Limits of Conservative Source Interpolation Methods Using a Low Mach Number Hybrid Aeroacoustic Workflow," *Journal of Theoretical and Computational Acoustics*, Vol. 29, No. 1, 2021, Paper 2050032. <https://doi.org/10.1142/S2591728520500322>
- [24] Schoder, S., Junger, C., Weitz, M., and Kaltenbacher, M., "Conservative Source Term Interpolation for Hybrid Aeroacoustic Computations,"



- 25th AIAA/CEAS Aeroacoustics Conference, AIAA Paper 2019-2538, 2019.  
<https://doi.org/10.2514/6.2019-2538>
- [25] Tautz, M., *Aeroacoustic Noise Prediction of Automotive HVAC Systems*, FAU Univ. Press, Erlangen, 2019.  
<https://doi.org/10.25593/978-3-96147-216-1>
- [26] Bogey, C., Gloerfelt, X., and Bailly, C., "Illustration of the Inclusion of Sound-Flow Interactions in Lighthill's Equation," *AIAA Journal*, Vol. 41, No. 8, 2003, pp. 1604–1606.  
<https://doi.org/10.2514/2.2115>
- [27] Samanta, A., Freund, J. B., Wei, M., and Lele, S. K., "Robustness of Acoustic Analogies for Predicting Mixing-Layer Noise," *AIAA Journal*, Vol. 44, No. 11, 2006, pp. 2780–2786.  
<https://doi.org/10.2514/1.22186>
- [28] Cheung, L. C., and Lele, S. K., "Linear and Nonlinear Processes in Two-Dimensional Mixing Layer Dynamics and Sound Radiation," *Journal of Fluid Mechanics*, Vol. 625, April 2009, pp. 321–351.  
<https://doi.org/10.1017/S0022112008005715>
- [29] Hiraishi, M., Tsutahara, M., and Leung, R., "Numerical Simulation of Sound Generation in a Mixing Layer by the Finite Difference Lattice Boltzmann Method," *Computers & Mathematics with Applications*, Vol. 59, No. 7, 2010, pp. 2403–2410.  
<https://doi.org/10.1016/j.camwa.2009.08.073>
- [30] Fortuné, V., Lamballais, E., and Gervais, Y., "Noise Radiated by a Non-Isothermal, Temporal Mixing Layer. Part I: Direct Computation and Prediction Using Compressible DNS," *Theoretical and Computational Fluid Dynamics*, Vol. 18, No. 1, 2004, pp. 61–81.  
<https://doi.org/10.1007/s00162-004-0114-8>
- [31] Kaltenbacher, M., Roppert, K., Schoder, S., and Heinz, J., "Stable Finite Element Formulation for the Perturbed Convective Wave Equation," *EuroNoise 2021*, EAA, 2021.
- [32] Freund, J. B., Lele, S. K., and Moin, P., "Numerical Simulation of a Mach 1.92 Turbulent Jet and its Sound Field," *AIAA Journal*, Vol. 38, No. 11, 2000, pp. 2023–2031.  
<https://doi.org/10.2514/2.889>
- [33] Crighton, D. G., "Basic Principles of Aerodynamic Noise Generation," *Progress in Aerospace Sciences*, Vol. 16, No. 1, 1975, pp. 31–96.  
[https://doi.org/10.1016/0376-0421\(75\)90010-X](https://doi.org/10.1016/0376-0421(75)90010-X)
- [34] Freund, J. B., "Noise-Source Turbulence Statistics and the Noise from a Mach 0.9 Jet," *Physics of Fluids*, Vol. 15, No. 6, 2003, pp. 1788–1799.  
<https://doi.org/10.1063/1.1569919>
- [35] Margnat, F., and Gloerfelt, X., "On Compressibility Assumptions in Aeroacoustic Integrals: A Numerical Study with Subsonic Mixing Layers," *Journal of the Acoustical Society of America*, Vol. 135, No. 6, 2014, pp. 3252–3263.  
<https://doi.org/10.1121/1.4875561>
- [36] Chu, B., and Kovásznyai, L. S. G., "Non-Linear Interactions in a Viscous Heat-Conducting Compressible Gas," *Journal of Fluid Mechanics*, Vol. 3, No. 5, 1958, pp. 494–514.  
<https://doi.org/10.1017/S0022112058000148>
- [37] Nana, C., Marx, D., Prax, C., and Fortuné, V., "Hybrid Aeroacoustic Computation of a Low Mach Number Non-Isothermal Shear Layer," *Computers & Fluids*, Vol. 93, April 2014, pp. 30–40.  
<https://doi.org/10.1016/j.compfluid.2014.01.006>
- [38] Yates, J. E., "Application of the Bernoulli Enthalpy Concept to the Study of Vortex Noise and Jet Impingement Noise," NASA CR 2987, Washington, D.C., 1978.
- [39] Perez Bergliaffa, S. E., Hibberd, K., Stone, M., and Visser, M., "Wave Equation for Sound in Fluids with Vorticity," *Physica D: Nonlinear Phenomena*, Vol. 191, Nos. 1–2, 2004, pp. 121–136.  
<https://doi.org/10.1016/j.physd.2003.11.007>
- [40] Leubner, C., "Coordinate-Free Interpretation of the Laplacian," *European Journal of Physics*, Vol. 8, No. 1, 1987, p. 10.  
<https://doi.org/10.1088/0143-0807/8/1/003>
- [41] Bogey, C., Bailly, C., and Juvé, D., "Computation of Flow Noise Using Source Terms in Linearized Euler's Equations," *AIAA Journal*, Vol. 40, No. 2, 2002, pp. 235–243.  
<https://doi.org/10.2514/6.2000-2047>
- [42] Zhou, L., Wan, Z., Sun, D.-J., and Wei, M., "Sound Generation by Different Vortex Interactions in Mixing Layers," *50th AIAA Aerospace Sciences Meeting Including the New Horizons Forum and Aerospace Exposition*, AIAA Paper 2012-1173, 2012.  
<https://doi.org/10.2514/6.2012-1173>
- [43] Golanski, F., Moser, C., Nadal, L., Prax, C., and Lamballais, E., "Numerical Methodology for the Computation of the Sound Generated by a Non-Isothermal Mixing Layer at Low Mach Number," *Direct and Large-Eddy Simulation VI*, Springer, Berlin, 2006, pp. 529–536.  
[https://doi.org/10.1007/978-1-4020-5152-2\\_61](https://doi.org/10.1007/978-1-4020-5152-2_61)
- [44] Moser, C., Lamballais, E., and Gervais, Y., "Direct Computation of the Sound Generated by Isothermal and Non-Isothermal Mixing Layers," *12th AIAA/CEAS Aeroacoustics Conference (27th AIAA Aeroacoustics Conference)*, AIAA Paper 2006-2447, 2006.  
<https://doi.org/10.2514/6.2006-2447>
- [45] Cabana, M., Fortuné, V., and Jordan, P., "Identifying the Radiating Core of Lighthill's Source Term," *Theoretical and Computational Fluid Dynamics*, Vol. 22, No. 2, 2008, pp. 87–106.  
<https://doi.org/10.1007/s00162-008-0075-4>
- [46] Wei, M., and Freund, J. B., "A Noise-Controlled Free Shear Flow," *Journal of Fluid Mechanics*, Vol. 546, Jan. 2006, pp. 123–152.  
<https://doi.org/10.1017/S0022112005007093>
- [47] Golanski, F., Fortuné, V., and Lamballais, E., "Noise Radiated by a Non-Isothermal, Temporal Mixing Layer," *Theoretical and Computational Fluid Dynamics*, Vol. 19, No. 6, 2005, pp. 391–416.  
<https://doi.org/10.1007/s00162-005-0002-x>
- [48] Colonius, T., Lele, S. K., and Moin, P., "Sound Generation in a Mixing Layer," *Journal of Fluid Mechanics*, Vol. 330, Jan. 1997, pp. 375–409.  
<https://doi.org/10.1017/S0022112096003928>
- [49] Bogey, C., Bailly, C., and Juvé, D., "Numerical Simulation of Sound Generated by Vortex Pairing in a Mixing Layer," *AIAA Journal*, Vol. 38, No. 12, 2000, pp. 2210–2218.  
<https://doi.org/10.2514/2.906>
- [50] Bogey, C., and Bailly, C., "A Family of Low Dispersive and Low Dissipative Explicit Schemes for Flow and Noise Computations," *Journal of Computational Physics*, Vol. 194, No. 1, 2004, pp. 194–214.  
<https://doi.org/10.1016/j.jcp.2003.09.003>
- [51] Bogey, C., De Cacqueray, N., and Bailly, C., "A Shock-Capturing Methodology Based on Adaptive Spatial Filtering for High-Order Non-Linear Computations," *Journal of Computational Physics*, Vol. 228, No. 5, 2009, pp. 1447–1465.  
<https://doi.org/10.1016/j.jcp.2008.10.042>
- [52] Berland, J., Bogey, C., Marsden, O., and Bailly, C., "High-Order, Low Dispersive and Low Dissipative Explicit Schemes for Multiple-Scale and Boundary Problems," *Journal of Computational Physics*, Vol. 224, No. 2, 2007, pp. 637–662.  
<https://doi.org/10.1016/j.jcp.2006.10.017>
- [53] Tam, C. K., and Dong, Z., "Radiation and Outflow Boundary Conditions for Direct Computation of Acoustic and Flow Disturbances in a Non-uniform Mean Flow," *Journal of Computational Acoustics*, Vol. 4, No. 2, 1996, pp. 175–201.  
<https://doi.org/10.1142/S0218396X96000040>
- [54] Bogey, C., and Bailly, C., "Three-Dimensional Non-Reflective Boundary Conditions for Acoustic Simulations: Far Field Formulation and Validation Test Cases," *Acta Acustica united with Acustica*, Vol. 88, No. 4, 2002, pp. 463–471.
- [55] Monkewitz, P. A., and Huerre, P., "Influence of the Velocity Ratio on the Spatial Instability of Mixing Layers," *Physics of Fluids*, Vol. 25, No. 7, 1982, pp. 1137–1143.  
<https://doi.org/10.1063/1.863880>
- [56] Schoder, S., Roppert, K., Weitz, M., Junger, C., and Kaltenbacher, M., "Aeroacoustic Source Term Computation Based on Radial Basis Functions," *International Journal for Numerical Methods in Engineering*, Vol. 121, No. 9, 2020, pp. 2051–2067.  
<https://doi.org/10.1002/nme.6298>
- [57] Schoder, S., Junger, C., Roppert, K., and Kaltenbacher, M., "Radial Basis Function Interpolation for Computational Aeroacoustics," *AIAA Aviation 2020 Forum*, AIAA Paper 2020-2511, 2020.  
<https://doi.org/10.2514/6.2020-2511>
- [58] Schoder, S., "Aeroacoustic Analogies Based on Compressible Flow Data," Ph.D. Thesis, TU Wien, Vienna, 2019.  
<https://doi.org/10.34726/hss.2018.40525>
- [59] Schoder, S., Roppert, K., and Kaltenbacher, M., "Helmholtz's Decomposition for Compressible Flows and Its Application to Computational Aeroacoustics," *SN Partial Differential Equations and Applications*, Vol. 1, No. 6, 2020, pp. 1–20.  
<https://doi.org/10.1007/s42985-020-00044-w>
- [60] Schoder, S., Roppert, K., and Kaltenbacher, M., "Postprocessing of Direct Aeroacoustic Simulations Using Helmholtz Decomposition," *AIAA Journal*, Vol. 58, No. 7, 2020, pp. 3019–3027.  
<https://doi.org/10.2514/1.J058836>
- [61] Schoder, S., Toth, F., Freidhager, C., and Kaltenbacher, M., "Revisiting Infinite Mapping Layer for Open Domain Problems," *Journal of Computational Physics*, Vol. 392, Sept. 2019, pp. 354–367.  
<https://doi.org/10.1016/j.jcp.2019.04.067>
- [62] Kaltenbacher, B., Kaltenbacher, M., and Sim, I., "A Modified and Stable Version of a Perfectly Matched Layer Technique for the 3-D Second Order Wave Equation in Time Domain with an Application to

- Aeroacoustics,” *Journal of Computational Physics*, Vol. 235, Feb. 2013, pp. 407–422.  
<https://doi.org/10.1016/j.jcp.2012.10.016>
- [63] Ainsworth, M., “Discrete Dispersion Relation for hp-Version Finite Element Approximation at High Wave Number,” *SIAM Journal on Numerical Analysis*, Vol. 42, No. 2, 2004, pp. 553–575.  
<https://doi.org/10.1137/S0036142903423460>
- [64] Martínez-Lera, P., and Schram, C., “Correction Techniques for the Truncation of the Source Field in Acoustic Analogies,” *Journal of the Acoustical Society of America*, Vol. 124, No. 6, 2008, pp. 3421–3429.  
<https://doi.org/10.1121/1.2999555>
- [65] Hilber, H. M., Hughes, T. J., and Taylor, R. L., “Improved Numerical Dissipation for Time Integration Algorithms in Structural Dynamics,” *Earthquake Engineering & Structural Dynamics*, Vol. 5, No. 3, 1977, pp. 283–292.  
<https://doi.org/10.1002/eqe.4290050306>
- [66] Ribner, H. S., “Aerodynamic Sound from Fluid Dilatations—A Theory of the Sound from Jets and Other Flows,” Inst. for Aerospace Studies, Univ. of Toronto, UTIA Rept. 86, AFOSR TN 3430, Toronto, 1962.
- [67] Taylor, G. I., “The Spectrum of Turbulence,” *Proceedings of the Royal Society of London: Series A—Mathematical and Physical Sciences*, Vol. 164, No. 919, 1938, pp. 476–490.  
<https://doi.org/10.1098/rspa.1938.0032>
- [68] Lighthill, M. J., “On Sound Generated Aerodynamically I: General Theory,” *Proceedings of the Royal Society of London*, Vol. 211, No. 1107, 1951, pp. 564–587.
- [69] Freund, J. B., “Noise Sources in a Low-Reynolds-Number Turbulent Jet at Mach 0.9,” *Journal of Fluid Mechanics*, Vol. 438, July 2001, pp. 277–305.  
<https://doi.org/10.1063/1.1569919>

X. Zhang  
Associate Editor